ISSN 0915-633X

NATIONAL INSTITUTE FOR FUSION SCIENCE

Monte Carlo Simulation Study of the ICRF Minority Heating in the Large Helical Device

S. Murakami, M. Okamoto, N. Nakajima, M. Ohnishi, H. Okada

(Received – Oct. 1, 1993)

NIFS-249 Oct. 1993

RESEARCH REPORT
NIFS Series

NAGOYA, JAPAN

MONTE CARLO SIMULATION STUDY OF THE ICRF MINORITY HEATING IN THE LARGE HELICAL DEVICE

S. MURAKAMI, M. OKAMOTO, N. NAKAJIMA

National Institute for Fusion Science,

Nagoya 464-01, Japan

M. OHNISHI

Institute of Atomic Energy,

Kyoto University,

Uji, Kyoto 611, Japan

H. OKADA

Plasma Physics Laboratory,

Kyoto University,

Uji, Kyoto 611

Keywords: Monte Carlo simulation, ICRF minority heating, the Large Helical Device, heat efficiency, finite beta effects

ABSTRACT

A Monte Carlo simulation code is developed for the ICRF heating in helical systems, which takes into account finite beta effects, complicated orbits of high energetic particles, Coulomb collisions, and interactions between the particles and the applied waves. The code is used to investigate the ICRF minority heating in the Large Helical Device. The configuration of the magnetic fields changes significantly due to finite beta effects in the Large Helical Device. The resonance layer position is found to be crucial to the heating efficiency as the plasma beta increases. When the strength of the resonance magnetic field is set to the value at the magnetic axis, the higher heat efficiency is obtained and no clear difference of the heat efficiency due to the finite beta effects is found at the high ICRF wave power region. However the radial profile of the transferred power to majority ions and electrons from minority ions changes by the deformation of the trapped particle orbits due to the finite beta effects. The heat efficiency is improved if the radial electric field, E_r, is positive (E_r is directed radially outward) and it is also improved by supplying ^{3}He minority ions rather than proton minority ions.

1. INTRODUCTION

The electromagnetic wave heating in the ion cyclotron range of frequencies (ICRF) has attracted much attention as an effective heating method and up to MW order of ICRF heating experiments have been performed not only in tokamaks but also in helical systems[1-4]. The theoretical studies of the ICRF heating in tokamaks have been done mainly by solving the Fokker-Planck equation. However, recently the importance of finite orbit effects in ICRF heatings of tokamak plasmas was pointed out[5,6] and it was shown that radial profiles of fast ions and depositions change substantially. In helical systems the study of the ICRF heating solving the Fokker-Planck equation was done by Fukuyama et al.[7] and their result suggests that the heating property is strongly influenced by the existence of loss cones for fast ions. Additionally, high energy particles produced by ICRF heating draw a complicated orbit because of the non-axisymmetric configuration[8-11] and these orbits of high energy particles would play an important role in the ICRF heating. Therefore the inclusion of effects of finite particle orbits is required to evaluate the more accurate heating efficiency in helical systems. The Monte Carlo simulation method is one of the useful methods to include these effects and has been applied to the analysis of the neutral beam injection heating in non-axisymmetric systems[12-16].

In this paper we study the ICRF heating of the plasma in the Large Helical Device (LHD)[17] using the Monte Carlo simulation code, MOMOCO, in which finite beta effects, complicated orbits of high energy particles, Coulomb collisions, and interactions between particles and the applied ICRF waves are included. The two ion component plasma which consists of electrons, majority ions, and minority ions is considered in the minority heating regime of ICRF heating. Choosing the small fraction of minority ions and the proper $k_{\|}$, almost all the wave energy is absorbed by minority ions through the ion cyclotron resonance. We treat deuteron as the majority ion and proton or ^{3}He as the minority ion. The stored energy in minority ions is transferred to majority ions and electrons

through particle Coulomb collisions and, then, the plasma is heated up. If all of the stored energy of minority ions is transferred to them the heating efficiency is considered to be unity. However. there exist some loss mechanism of stored energy of minority ions, e.g. the orbit loss and charge exchange loss. In a helical system the dominant mechanism losing the stored energy in minority ions is the orbit loss of particles. Thus, we consider only the dominant effect, i.e. the orbit loss, in the present paper. The loss boundary of the particle confinement is given by the last closed magnetic surface of the equilibrium. This assumption might over-count the loss of the particles and the extension of the loss boundary to the vacuum vessel is need for further studies. In that case, however, the large increment of the charge exchange loss of minority ions would occur and there also needs to incorporate the effects of the charge exchange loss[13.16].

The magnetic configuration of LHD is calculated by the three dimensional magnetohydrodynamic (MHD) equilibrium code, VMEC[18]. Magnetic surfaces of the LHD plasma are deformed due to large Shafranov shift with increasing the plasma beta, resulting in large changes in particle orbits. Changing the plasma beta we investigate the plasma beta effects on the ICRF minority heating.

Effects of the radial electric field is also studied. In helical systems the radial electric field, E_r, much affects particle motions not only at the plasma periphery but also near the center of plasma[9,10]. Here we introduce a model E_r field and study the effects on the ICRF heating. It should give us a clue to make clear the relation between the ICRF heating and the radial electric field, E_r.

The magnetic configuration of the LHD to be studied is shown in Section 2. In section 3 the orbit following part, Monte Carlo collision operator, and ICRF heating model are explained. The results from calculations are shown in section 4. Firstly we show the finite beta effects and, secondly the influence of the radial electric field and the species of minority ions are shown. Conclusion is given in section 5.

2. MAGNETIC CONFIGURATION OF THE LARGE HELICAL DEVICE

In this paper we study the ICRF heating of the plasma in the Large Helical Device (LHD) for the magnetic configuration obtained as follows. First we calculate the vacuum magnetic field using the actual coil parameters of the LHD. The main parameters of LHD are given in Table I. Controlling the axisymmetric poloidal fields, we can move the plasma horizontally to shift the magnetic axis position inward or outward relative to the center of helical coils. We can also add the ellipiticity to the magnetic surfaces adjusting the poloidal fields. We, here, introduce the LHD configuration called "the standard configuration"[17] in which the shift of the vacuum magnetic axis position, Δ, is -0.15m (0.15m inward shift) and the toroidally averaged magnetic surfaces are nearly circular in the vacuum field. This configuration satisfies the requirements for high plasma performance, i.e. a good bulk particle confinement, a high plasma beta, and creating a divertor configuration.

Using the vacuum magnetic field configuration, we solve the three dimensional finite beta MHD equilibrium by the VMEC code[18] under the fixed boundary condition. We assume the pressure profile, P, as $P = P_0(1 - \overline{\psi})^2$ where $\overline{\psi}$ is the normalized toroidal flux.

Based on the obtained MHD equilibrium we construct the Boozer coordinates (ψ, θ, ϕ), where ψ is the toroidal flux divided by 2π, and θ and ϕ are poloidal and toroidal angle, respectively. In this step we select dominant poloidal and toroidal Fourier modes of the magnetic strength B. Because the numbers of Fourier modes of the magnetic configuration in the constructed Boozer coordinates amounts to more than 1000, it is not convenient to calculate particle motions with all the modes. The dominant modes are selected by the condition, $|B_{m,n}(\psi)| \,/\, |B_{max}(\psi)| \geq \varepsilon_c$, where B_{max} is the maximum mode amplitude except $B_{0,0}$ on the magnetic surface with a label of ψ and ε_c is a critical parameter of mode selection to be specified. Evaluation of this condition is done at the each ψ surface and if a mode satisfies this condition at least at one ψ surface this mode is included in the

all ψ surfaces. Table II shows the number of selected modes in terms of plasma beta at the axis, β_0, when $\varepsilon_c = 1.0 \times 10^{-3}$. The rapid increase in the number of selected modes shows that the configuration becomes more complicated with increasing beta.

Figure 1 shows the contour of the magnetic field strength in the Boozer coordinates. We show the four beta value cases, $\beta_0 = 0.0, 2.0, 4.0, 6.0\%$, with three different toroidal angles, $\phi = 0.0, 1/4 \times 2\pi/m$ and $2/4 \times 2\pi/m$ where $m(= 10)$ is the toroidal pitch number shown in Table I. In the real coordinates these magnetic surfaces indicate the longitudinally elongated shape for the toroidal angle $\phi = 0.0$ and the laterally elongated shape for $\phi = 2/4 \times 2\pi/10$. Significant changes in the magnetic configuration are attributed to large Shafranov shifts due to the finite beta effects. Figure 2 shows the contours of mod-B_{min} which approximately give the orbits of deeply trapped particles[19]. In Fig. 2 magnetic surfaces are concentric circles (not shown) and it is seen that the contours deviate from the magnetic surfaces more and more as β_0 increases. This means that the confinement of deeply trapped particles becomes worse with increasing beta. This fact suggests that motions of trapped particles as well as transition particles are more complicated in higher beta plasma.

3. NUMERICAL PROCEDURE

In order to study the ICRF minority heating taking into account the complicated motions of minority ions, Coulomb collisions of minority ions with majority ions and electrons, and interactions of minority ions with the ICRF wave, we develop a Monte Carlo simulation code "MOMOCO". This code mainly consists of three parts; particle orbit following part, particle collision part, and ICRF heating part.

In the particle orbit following part we solve the equation of motion in the Boozer coordinates. Starting from the Hamiltonian of charged particle,

$$H = \frac{1}{2} m v_{\parallel}^2 + \mu B + q\Phi, \tag{1}$$

where m, q, $v_{\|}$ and μ are the mass, the charge, the parallel velocity and the magnetic moment of the particle, respectively, we can obtain equations of motion in terms of the Boozer coordinates at finite plasma beta, which are given by[20]

$$\dot{\psi} = -\left(g\frac{\partial B}{\partial \theta} - I\frac{\partial B}{\partial \phi}\right)\frac{\delta}{\gamma}, \tag{2}$$

$$\dot{\rho_c} = \left[(\rho_c g' - \iota)\frac{\partial B}{\partial \theta} - (\rho_c I' + 1)\frac{\partial B}{\partial \phi}\right]\frac{\delta}{\gamma}, \tag{3}$$

$$\dot{\theta} = \left(\delta\frac{\partial B}{\partial \psi} + q\frac{\partial \Phi}{\partial \psi}\right)\frac{g}{\gamma} - \frac{q^2B^2\rho_c}{m}\cdot\frac{(\rho_c g' - \iota)}{\gamma}, \tag{4}$$

$$\dot{\phi} = -\left(\delta\frac{\partial B}{\partial \psi} + q\frac{\partial \Phi}{\partial \psi}\right)\frac{I}{\gamma} + \frac{q^2B^2\rho_c}{m}\cdot\frac{(\rho_c I' + 1)}{\gamma}, \tag{5}$$

where

$$\gamma = q[g(\rho_c I' + 1) - I(\rho_c g' - \iota)], \tag{6}$$

$$\delta = q^2\rho_c^2 B/m + \mu, \tag{7}$$

and ψ is the toroidal flux divided by 2π, $\rho_c = mv_{\|}/qB$, and θ and ϕ are the poloidal and toroidal angles, respectively. $I(\psi)$ is the toroidal current within a flux surface, $g(\psi)$ is the poloidal current outside a flux surface and ι is the rotational transform. We solve the time development of eqs. (2) to (5) with high accuracy.

In order to take into account Coulomb collisions of minority ions with majority ions and electrons we introduce the Monte Carlo collision operator based on the binominal distribution[21]. The pitch angle scattering by the particles of species s after the time interval Δt is given in terms of λ, $\lambda = v_{\|}/v$, by

$$\lambda_{n+1} = \lambda_n(1 - \nu_{ds}\Delta t) + \sigma[(1 - \lambda_n^2)\nu_{ds}\Delta t]^{1/2}, \tag{8}$$

where σ takes $+1$ or -1 with equal probabilities. ν_{ds} is the deflection collision frequency written by

$$\nu_{ds} = \frac{3}{2}\left(\frac{\pi}{2}\right)^{1/2}\nu_{Bs}\frac{\Phi(x) - \Psi(x)}{x^3}, \tag{9}$$

$$\Phi(x) = \frac{2}{\sqrt{\pi}}\int_0^x \exp(-t^2)dt, \tag{10}$$

$$\Psi(x) = (\Phi - x\Phi')/2x^2, \tag{11}$$

where $x = v/v_{ths}$ and v_{ths} is the thermal velocity of the background particles of species s ($s =$ i or e). ν_{Bs} is the Braginskii collision frequency,

$$\nu_{Bs} = \frac{4}{3}\left(\frac{\pi}{m_s}\right)^{1/2} \frac{\Lambda_s q_s^4 n_s}{T_s^{3/2}}, \tag{12}$$

where Λ_s is the Coulomb logarithm, and q_s, n_s, and T_s are the charge, the density, and the temperature of the background particles of species s, respectively. The energy scattering after the time interval Δt is given by

$$E_{n+1} = E_n - (2\nu_{Es}\Delta t)\left[E_n\left(\frac{3}{2} + \frac{E_n}{\nu_{Es}}\frac{d\nu_{Es}}{dE}\right)T_s\right] + \sigma 2[T_s E_n(\nu_{Es}\Delta t)]^{1/2}, \tag{13}$$

where

$$\nu_{Es} = 3(\pi/2)^{1/2}\nu_{Bs}[\Psi(x)/x]. \tag{14}$$

In this collision operator we decide the time step, Δt, to satisfy the condition , $\nu_{ds}\Delta t << 1$. We calculate the pitch angle scattering and energy scattering of minority ions by the two species, i.e. majority ion and electron, in every time step.

When a minority ion passes through the ion cyclotron resonance layer the particle interacts with the ICRF waves to change its velocity. The resonance condition is given by

$$\omega - k_\parallel v_\parallel = n\Omega, \tag{15}$$

where ω and $k_\parallel$ are the frequency and the parallel wave number of the applied ICRF wave, respectively. $v_\parallel$ and Ω are the parallel velocity and the cyclotron frequency, $\Omega = qB/m$, of the minority, respectively. Assuming $k_\parallel \simeq 0$, the change in the velocity occurs in the perpendicular direction and is given by[22]

$$\Delta v_\perp = \frac{q}{2m} I\, e^{-in\phi_r}\left[|E_+|\ J_{n-1}(k_\perp\rho) + |E_-|\ J_{n+1}(k_\perp\rho)\right] \tag{16}$$

where ρ is the larmor radius, $\rho = mv_\perp/qB$, and J_n is the n-th Bessel function of the first kind. ϕ_r is the phase of the ICRF wave which is treated as uniform random between 0 to 2π and I is the function related to the resonance duration time. When the turning point

dose not close to the resonance layer I is written as $I = \sqrt{2\pi/n\dot{\Omega}}$ where $\dot{\Omega}$ is the time derivative of Ω, $\dot{\Omega} = q/m(\boldsymbol{v}\cdot\nabla)\boldsymbol{B}$. As the turning point comes very near the resonance layer $\dot{\Omega}$ becomes zero ($v_{\parallel} \simeq 0$) and the higher order correction in terms of $\ddot{\Omega}$ should be included. That is expressed [5,23,24] as $I = 2\pi[n\ddot{\Omega}/2]^{-1/3}Ai(0)$, where Ai is the Airy function. However we introduce the more simplified model in which I takes the constant value when the turning point closes to the resonance layer. The obtained results, e.g. heat efficiency, transferred power and etc., for the two models show good agreements and we here use the simplified model when the turning point closes th the resonance layer in the following calculations.

Further assuming $k_{\perp}\rho \simeq 0$ and $n = 1$, we obtain

$$\Delta v_{\perp} = \frac{qE_{RF}}{2m} I\, e^{-i\phi_r}. \tag{17}$$

We assume that the applied wave electric field on the resonance layer, $E_{RF}(= |E_{+}|)$, is uniform over the resonance layer and fixed in time.

In order to study the influence of the radial electric field we introduce a model radial electric field which is expressed as

$$E_r(\psi) = -\frac{\partial\Phi(\psi)}{\partial r}, \tag{18}$$

$$\Phi(\psi) = \Phi_0(1-\overline{\psi})^2. \tag{19}$$

We use $1000 \sim 3000$ particles and assume that initially all the minority ions form a Maxwellian distribution in the velocity space;

$$f(v) = \frac{N}{(2\pi)^{3/2}v_{th}^3}\exp[-v^2/2v_{th}^2], \tag{20}$$

where N is the total number of minority ions used in the calculations. In Eq. (20), v_{th} is the thermal speed of initially loaded minority ions with a constant temperature of 1.0 keV . Pitch angles of the minority ions are randomly distributed. The minority ions are initially loaded in the real space by

$$n(\overline{\psi}) = n_{m0}\exp[-c\overline{\psi}^2], \tag{21}$$

where $\overline{\psi} = \psi/\psi_a$ (ψ_a is the flux function on the last closed flux surface). Note that ψ is proportional to r^2, where r is the average minor radius. n_{m0} is the density of minority ions at the axis ($\psi = 0$) and c is the inverse of the standard deviation, set to be 4 in the present paper. The particles are randomly distributed in the θ and ϕ space.

Minority ions are accelerated on average by the waves and heat the majority ions and electrons through Coulomb collisions. Therefore temperatures of majority ions and electrons change during the development of ICRF heating. However, we fix the density and temperatures of majority ions and electrons during the calculations for simplicity. The distribution of majority ions and electrons are given by

$$n_i(\psi) = n_e(\psi) = n_0(1-\overline{\psi})^{a_1}, \tag{22}$$

$$T_e(\psi) = T_{e0}(1-\overline{\psi})^{a_2}, \tag{23}$$

$$T_i(\psi) = T_{i0}(1-\overline{\psi})^{a_3}, \tag{24}$$

where n_i and n_e are the density of majority ions and electrons, respectively, and T_i and T_e are the temperature of majority ions and electrons, respectively. We set the parameters as $n_0 = 1.0 \times 10^{20}\mathrm{m}^{-3}$, $T_{e0} = 1.0\mathrm{keV}$, $T_{i0} = 1.0\mathrm{keV}$ and $a_1 = a_2 = a_3 = 2$. This simple model enables us to gain an insight about basic physics lying under the ICRF heating.

4. RESULTS

4.1 Effects of Finite Beta

We perform a large number of simulation runs changing the plasma beta, the strength of wave electric field, E_{RF}, and the position of resonance layer. First we show the time development of our simulation for a typical case of parameters; $\beta_0 = 0.0\%$, $E_{RF} = 2.5 \times 10^3\mathrm{V/m}$, and $\Phi = 0.0\mathrm{eV}$. The strength of the resonance magnetic field is set to the value at the magnetic axis. Figure 3-(a) shows the time development of averaged total energy of minority ions (solid line) and perpendicular one (dashed line). Initially the pitch angle

of the minority ions are randomly distributed form 0 to π. Most of particles ($\sim 80\%$) are circulating particles at the first stage of the time development. Circulating particles move nearly along a magnetic field line and change the perpendicular velocity by the amount of $\Delta v_\perp$ given by Eq. (17) whenever they pass through the ion cyclotron resonance layer. The particles gain energy perpendicular to the magnetic field with time and the pitch angles of the particles are increased. Then the particles turn into trapped particles. From this figure we can see the rapid increase of the average energy and the rapid production of the high energy tail of minority ions during the first 1ms. In contrast with it, around 10ms the average energy of minority ions seems to be saturated, because the absorbed ICRF wave power by minority ions, P_{abs}, is balanced with the other two powers; the power transferred to majority ions and electrons, P_{trans}, and the power lost by the orbit losses of minority ions, P_{loss}. Here, we define the absorbed power, P_{abs}, by

$$P_{abs} = \xi \sum_{i=1}^{M} \Delta E_i \tag{25}$$

where ΔE_i is the energy change given by Eq. (17), M is the number of times passing through the resonance layer of minority ions per unit time. ξ is a factor to translate the value obtained by the simulation into that of real plasma and is given by N_{min}/N_{MC}, where N_{min} is the actual numbers of minority ions in the plasma and N_{MC} is the numbers of minority ions used in the Monte Carlo simulations. In order to evaluate the value of ξ, we must specify the fraction of minority ions in the plasma which is determined based on the relation between the absorption power and the strength of wave electric field in the real plasma. Throughout the paper we assume that the fraction of minority ions is 3%[25]. Other powers, P_{trans} and P_{loss} are defined in a similar way.

The absorbed power, P_{abs}, changes during the time development. It is large at the initial stage ($t \leq$ 1ms) because of the relatively small $v_\parallel$ and the large fraction of circulating particles which frequently pass through the resonance layer (M in Eq.(25) is large). After 2 or 3ms the particle energy rises and the fraction of trapped or transition particles increases, resulting in smaller P_{abs}. Finally P_{abs} becomes close to a constant value. Fig. 3-(b) shows

the time development of the total absorption energy to minority ions, $\int P_{abs}\mathrm{d}t$, (solid line) and the total transferred energy, $\int P_{trans}\mathrm{d}t$, (dotted line). The dashed line shows the fraction of the transferred energy in the reduction of the minority ion energy and we can see no remarkable change in the fraction of transfer energy when $t \geq 4$ms. Hereafter we discuss the heating efficiency using the saturated value shown here.

We consider the finite beta effects on the ICRF minority heating changing the plasma beta value at the center, β_0, from 0.0% to 6.0%. We show the radial profile of the transferred power from minority ions to majority ions and electrons. Figure 4 shows the comparison of P_{trans} between (a) the $\beta_0 = 0.0\%$ case and (b) $\beta_0 = 6.0\%$ case. In both cases the strengths of the resonance magnetic field are set to the value at the magnetic axis and the strengths of wave electric field, E_{RF} are fixed to $E_{RF} = 2.5 \times 10^3$V/m. The closed circles show the transferred power to majority ions and the open circles are that to electrons. In both cases the transferred powers to electrons are larger than those of ions. This is because many of minority ions are accelerated up to a larger energy than the critical energy[26] $E_c \sim 10$ keV and minority ions heat mainly electrons.

The significant difference of radial profile can be seen between the two cases. In the case of $\beta_0 = 0.0$, the profile has a peak near the center and decreases roughly monotonically with r. On the other hand two peaks of P_{trans} are found in the case of $\beta_0 = 6.0\%$.

Figure 5 shows the projection of the typical particle orbits on the poloidal cross section for two different β_0 values and pitch angles. The particle collisions and the interaction with ICRF wave are not applied. It is found that the orbits of the deeply trapped particles (Fig. 5-(a) and (c)) agree well with the B_{min} contour lines in Fig. 2. From this figure the excursion of the deeply trapped particle from the original magnetic surface would enhance the power transfer not only at the center region but also at the plasma periphery in the case of $\beta_0 = 6.0\%$. Additionally, the behavior of the transition particles in the case of $\beta_0 = 6.0\%$ (Fig. 5- (d)), which is different from that of the $\beta_0 = 0.0\%$ case (Fig. 5- (b)), would also contribute to the formation of two peaks. In the case of $\beta_0 = 0.0\%$ (Fig. 5-

(b)) the transition from helically trapped particle to circulating particle occurs and the circulating particle moves outward (the center of the torus is located on the left side of the Figures). Thus, the circulating particle crosses the different B_{min} contours in Fig. 2 at the transition point. On the other hand, in the case of $\beta_0 = 6.0\%$ the two types of transition are found and the particles does not shift on the different B_{min} contour so much (Fig. 5-(d)), which leads to keeping the resonance with the RF wave in the same orbit of B_{min}. Therefore, in the case of $\beta_0 = 6.0\%$, the high energy particles would be distributed near the B_{min} region where magnetic field strength is equal to the resonance magnetic field. Then the transferred power from minority ions is also enhanced near that region. As a result the radial profile of the transferred power has two peaks in r (see the radial position of the B_{min} line of the resonance magnetic field strength in Fig. 2). On the other hand, in the case of $\beta_0 = 0.0\%$, because of the change of B_{min} during the transition the distribution of high energy particles would have a broader profile. Thus the radial profile of the transferred power does not have two peaks. Note that the radial profile of P_{trans} highly depend on the nature of the transition particles.

We show next the finite β effect on the heating efficiency of the ICRF minority heating. We introduce the transfer rate which is defined by P_{trans}/P_{abs} as a measure of the heating efficiency. Figure 6 shows the plots of transfer rates versus P_{abs}. The strengths of the resonance magnetic field are set to the value at the magnetic axis. The absorption power is changed by changing the RF electric field on the resonance layer from $E_{RF} = 1.0 \times 10^3$V/m to $E_{RF} = 3.0 \times 10^3$V/m in this Figure. In the case of $\beta_0 = 0.0\%$, the transfer rate is 92% for $P_{abs} = 2$MW and decreases monotonically with increasing in P_{abs}. For finite β values ($\beta_0 = 4.0$ and 6.0%) the transfer rates are around 70% when $P_{abs} \leq 5$MW. However, no remarkable differences in transfer rates are found for different β values ($\beta_0 = 0.0$, 2.0, 4.0, 6.0%) in the region of high absorption power ($P_{abs} > 5$MW).

We study the influence of the position of resonance layer on the transfer rate changing the applied wave frequency, f_0. Assuming $k_{\parallel} \simeq 0$ we find that the resonance layer cor-

responds to the isosurface of the strength of magnetic field defined by $B_{res} = 2\pi fm/q$. Hereafter we use B_{res} to express the position of the resonance layer. We vary B_{res} from 2.8T to 3.2T. Figure 7 show the influence of the resonance layer position on the transfer rate. Closed circles, triangles, and squares (or solid, dashed, and broken lines) are the results for $B_{res} = B_{axis}$. In the case of $\beta_0 = 0.0\%$ the transfer rate does not change so much even if B_{res} deviates from B_{axis}. However, as indicated by open triangles and squares in Fig. 7, the transfer rates are reduced if the position of the resonance layer is moved from the layer with $B_{res} = B_{axis}$. In addition to this fact it is found that the absorption power, P_{abs} changes according to the position of resonance layer. For instance, in the $\beta_0 = 6\%$ case, $P_{abs} = 4, 6$, and 12MW for $B_{res} = 3.2$, $2.8(B_{axis})$, and 3.0T, respectively, for the same strength of the RF electric field, E_{RF}.

4.2 Influence of radial electric field on the ICRF heating

In this section we study the influence of the radial electric field on the ICRF heating. The model field given by Eqs. (18) and (19) are employed. The introduction of the radial electric field adds the $E \times B$ drift to the particle motion. When the directions of $E \times B$ drift, $V_{E\times B}$, and the ∇B drift motion, $V_{\nabla B}$, are the same, the confinement of trapped particles is improved, while it deteriorates if they are opposite. In the case of $|V_{E\times B}| >> |V_{\nabla B}|$ the particle confinement is improved regardless of both directions. Even for circulating particles the $E \times B$ drift may affect their confinement[13].

The plots of the transfer rate for the different electric potential values are shown in Fig. 8. Closed circles, triangles, and squares (or solid, dashed, and broken lines) show the transfer rates for $\beta_0 = 0.0$, 4.0, 6.0% respectively when $\Phi_0 = 0$. Open circles, triangles, and squares are transfer rates with radial electric fields of $\Phi_0 = -1.0$keV, +1.0keV, and +5.0keV. It is seen from Fig. 8 that the transfer rates are improved if $\Phi_0 > 0$ ($E_r > 0$) and deteriorate if $\Phi_0 < 0$ ($E_r < 0$).

Figure 9 shows the orbits of deeply trapped particle based on the mod-B_{min} contours.

In the case of $\Phi_0 > 0$ the orbits approach concentric circles to be well confined. On the other hand the orbits of deeply trapped particles are largely deformed in the case of $\Phi_0 < 0$ and the fraction of unclosed orbits is increased. Thus the better confinement of deeply trapped particles are obtained in the $\Phi_0 > 0$ case and the confinement deteriorates in the $\Phi_0 < 0$ case. As a result the higher transfer rate is found in the $\Phi_0 > 0$ case.

When we compare the changes in the transfer rates of the finite β case with those of $\beta_0 = 0.0\%$ case due to the radial electric field the larger changes are found in the finite β case. This comes from the fact that the distorted orbits of helically trapped particles are reformed to improve their confinement by the $E \times B$ drift. In Fig. 9 the orbits of $\beta_0 = 6.0\%$ case are reformed better than those of $\beta_0 = 0.0\%$ case.

4.3 Influence of the species of minority ion

In this section we consider ^{3}He ions as minority ions to compare the result with that of proton minority ions. In the ^{3}He minority case the improvement of the transfer rate is expected because of the relatively short mean free path and small larmor radius. The comparison of the results between proton and ^{3}He minority cases is shown in Fig. 10. Large increases in P_{abs} are found in all ^{3}He cases (open circles, triangles, and squares) and these values are nearly two times larger than those of the proton minority case (closed circles, triangles, and squares) for the same E_{RF}. Assuming the same temperatures for two species of minority ions we can evaluate the ratio of P_{abs} by Eq. (17) to be $P_{abs}(^3\mathrm{He})/P_{abs}(\mathrm{proton}) \simeq 1.86$ which agrees with the simulation results.

The decreases of the number of lost minority ions are found in all β_0 case. In the $\beta_0 = 0.0\%$ case the orbit loss decreases by 10% compared to the proton case and that decrease is larger when the plasma beta is increased. In the $\beta_0 = 6.0\%$ case the orbit loss is less than that in proton case by 30%.

Transfer rates are improved in the ^{3}He minority case by a factor of $1.3 \sim 1.5$. That is due to the increase in collisions of minority ions with majority ions and electrons and the

decrease in orbit losses.

The radial profile of the transferred power to the majority ions and electrons are shown in Fig. 11; (a) $\beta_0 = 0.0\%$ and (b) $\beta_0 = 6.0\%$. Comparing with the proton minority case large increases in the transferred power to majority ions are found in both cases. This is explained by the increase in the critical energy, E_c. In the proton minority case the critical energy is $E_c \simeq 10$ keV near the plasma center and energy of protons flows mainly to electrons, while in the ^{3}He minority case the critical energy is $E_c \simeq 27$ keV near the plasma center and the partition to ions becomes large. The critical energy, E_c, is roughly proportional to the electron temperature and decreases with r. Thus the reduction of the transfer power to ions is found in the periphery of the plasma.

5. CONCLUSION

We have investigated the ICRF minority heating in the LHD plasma using the Monte Carlo simulation code, MOMOCO, in which finite beta effects, complicated orbits of high energetic particles, Coulomb collisions, and interactions between particles and the applied waves are included. The three dimensional MHD equilibrium is calculated by the VMEC code and the particle orbits are followed in the Boozer coordinates according to the equilibrium.

We have firstly shown the Monte Carlo simulation results for the time development of the minority ion heating in a helical system. The average energy of minority ions increases rapidly and a saturation of the average energy appears. In this saturated state the absorption power of the minority ions from ICRF wave, P_{abs}, balances with the sum of the power transferred to majority ions and electrons, P_{trans}, and the power lost by the orbit losses of minority ions, P_{loss}. The finite beta effects on the radial profile of the transferred powers to majority ions and electrons have been investigated. The clear change in the radial profile of transferred power can be seen when the plasma beta is increased. This

comes from the deformation of the trapped particle orbits due to the finite beta effects. The finite beta effects on the heating efficiency have been studied. It has been shown that the heating efficiency decreases with increasing plasma beta, but the efficiencies are not changed so much for different betas if the ICRF power is high. The dependency of the heating efficiency on the resonance layer position is also found due to the finite beta effects and the maximum heating efficiency is given when the resonance magnetic field strength is adjusted to the strength at the magnetic axis. The influence of radial electric field on the ICRF heating has been studied. The introduction of the radial electric field E_r improves the heat efficiency when E_r is positive (E_r is directed radially outward). It has been also found that the heat efficiency for the ^{3}He minority case is up to 30% higher than that of the proton minority case.

In the present paper we have assumed constant temperatures of majority ions and electrons. However majority ions and electrons are heated by the slowing down process of accelerated minority ions and this process is affected by the change in temperatures. It will be one way to incorporate the Monte Carlo code with a plasma transport code to treat the temperatures consistently. We have assumed $k_{\|} \simeq 0$, $k_{\perp}\rho << 1$, constant E_{RF} over the resonance layer, and neglecting right hand circulating electric field of the ICRF wave for simplicity. Another problem to be solved is the influence of escaping fast ions on creating a radial electric field. The radial electric field, then, changes the loss cone structures for fast ions. Thus it is necessary to determine the radial electric field consistently by including fast ion radial losses. These problems are under investigation.

ACKNOWLEDGEMENTS

The authors wish to thank Prof. T. Mutoh, Dr. A. Fukuyama, Dr. K. Ichiguchi, and Dr. K. Y. Watanabe for useful discussions. They also thank Prof. A. Iiyoshi and Prof. T. Sato for continuous encouragement. The calculations were carried out on the super computer SX-3 at the National Institute for Fusion Science.

REFERENCES

[1] MUTOH, T., et al., Nucl. Fusion **24** (1984) 1003.

[2] MUTOH, T., et al., in Plasma Physics Controlled Nuclear Fusion Research 1986 (Proc. 11th Int. Conf. Kyoto, 1986), Vol. 2, IAEA, Vienna (1987) 473.

[3] KWON, M., et al., Nucl. Fusion **32** (1992) 1225.

[4] BAKAEV, V.V., et al., in Plasma Physics Controlled Nuclear Fusion Research 1984 (Proc. 10th Int. Conf. London, 1984), Vol. 2, IAEA, Vienna (1985) 397.

[5] KOVANEN,M.A., et al., Nucl. Fusion **32** (1992) 787.

[6] KOVANEN,M.A., Nucl. Fusion **32** (1992) 945.

[7] FUKUYAMA, A., et al., Nucl. Fusion **26** (1986) 151.

[8] MYNICK, H.E., Phys. Fluids **26** (1983) 1008.

[9] ITOH, K., et al., Nucl. Fusion **29** (1989) 1851.

[10] ITOH, K., et al., Phys. Fluids B **3** (1991) 1294.

[11] TODOROKI, J., J. Phys. Soc. Jpn. **59** (1990) 2758.

[12] HANATANI, K., et al., Nucl. Fusion **21** (1981) 1067.

[13] HANATANI, K., PENNINGSFELD, F.-P., Nucl. Fusion **32** (1992) 1769.

[14] MORRIS, R.N., et al., Fusion Technol. **12** (1987) 281.

[15] FOWLER, R.H., et al., Fusion Technol. **20** (1991) 200.

[16] FOWLER, R.H., et al., Nucl. Fusion **30** (1990) 997.

[17] IIYOSHI, A., et al., Fusion Technol. **17** (1990) 148.

[18] HIRSHMAN, S.P., WHITSON, J.C., Phys. Fluids **26** (1983) 3553.

[19] GALEEV, A.A., SAGDEEV, R.Z., Review of Plasma Physics, (LEONTOVICH, M.A., Ed.), Vol. 7, Consultants Bureau, New York, London, 257.

[20] FOWLER, R.H., et al., Phys. Fluids **28** (1985) 338.

[21] BOOZER, A.H., KUO-PETRAVIC, G., Phys. Fluids **24** (1981) 851.

[22] STIX, T.H., Nucl. Fusion 15 (1975) 737.

[23] BERNSTEIN, I.B., BAXTER, D.C., Phys. Fluids **24** (1981) 108.

[24] KERBEL, G.D., McCOY, M.G., Phys. Fluids **28** (1985) 3629.

[25] MUTOH, T., personal communication, 1993.

[26] GAFFEY,Jr. , J.D., J. Plasma Phys. **16** (1976) 149.

TABLE I. PARAMETERS OF THE LHD

number of helical coil l	2
number of field period m	10
number of pairs of poloidal field coils	3
major radius R	3.9m
minor radius a	0.56m
pitch modulation parameter of winding law α	0.1
shift of magnetic axis Δ	-0.15m
strength of central magnetic field B_0	3.0T

TABLE II. NUMBER OF FOURIER COMPONENT

β_0 [%]	0.0	2.0	4.0	6.0
number of modes	33	42	55	114

FIGURE CAPTIONS

FIG. 1. Contour lines of the magnetic field strength of the finite beta LHD configurations in the Boozer coordinates. The bold lines show the contour lines of B=3.0T.

FIG. 2. Mod-B_{min} contours of the finite beta LHD configurations in the Boozer coordinates. The bold lines show the contour lines of B_{min}=3.0T.

FIG. 3. Time development of the minority ion heating; (a) averaged total energy (solid line) and averaged perpendicular energy (dashed line) and (b) the time development of the absorption energy of minority ions (solid line) and the transferred energy to background particles (dotted line). The dashed line shows the transfer rate.

FIG. 4. Comparison of the transferred energy to majority ions and electrons for two different plasma beta; (a) $\beta_0 = 0.0\%$ and (b) $\beta_0 = 6.0\%$ and other parameters are $E_{RF} = 2.5 \times 10^3$V/m and $\Phi_0 = 0$. The closed circles show the transferred power to majority ions and the open circles are that to electrons.

FIG. 5. Typical orbits of trapped particle in LHD. (a) and (b) shows the typical orbits of deeply trapped particle and transition particle in the case of $\beta_0 = 0.0\%$, respectively, and (c) and (d) are those in the case of $\beta_0 = 6.0\%$, respectively. We consider the 50keV protons and the particle collisions and interaction with ICRF wave are not included.

FIG. 6. Plots of the power transfer rate with changing the plasma beta and the strength of the electric field of RF wave. Closed circles, triangles, and squares (or solid, dashed, and broken lines) show the results of $\beta_0 = 0.0, 4.0$, and 6.0%, respectively.

FIG. 7. Influence of the resonance layer position on the transfer rate. Closed circles, triangles, and squares (or solid, dashed, and broken lines) show the results of $B_{res} = B_{axis}$ and open circles, triangles, and squares show the results of $B_{res} \neq B_{axis}$.

FIG. 8. Influence of the radial electric field on the transfer rate. Closed circles, triangles, and squares (or solid, dashed, and broken lines) show the results of $\Phi_0 = 0$ and open circles, triangles, and squares show the results with radial electric field.

FIG. 9. Orbits of deeply trapped particle with radial electric field based on the mod-B_{min} contours; (a) $\beta_0 = 0.0\%$ case and (b) $\beta_0 = 6.0\%$ case.

FIG. 10. Comparison of the results between proton and ^{3}He cases. Closed circles, triangles, and squares (or solid, dashed, and broken lines) show the results of proton minority case and open circles, triangles, and squares show the results of ^{3}He minority case.

FIG. 11. Radial profile of the transferred power to majority ions and electrons for ^{3}He minority case; (a) $\beta_0 = 0.0\%$ and (b) $\beta_0 = 6.0\%$ and other parameters are $E_{RF} = 2.5\times10^3$V/m and $\Phi_0 = 0$.

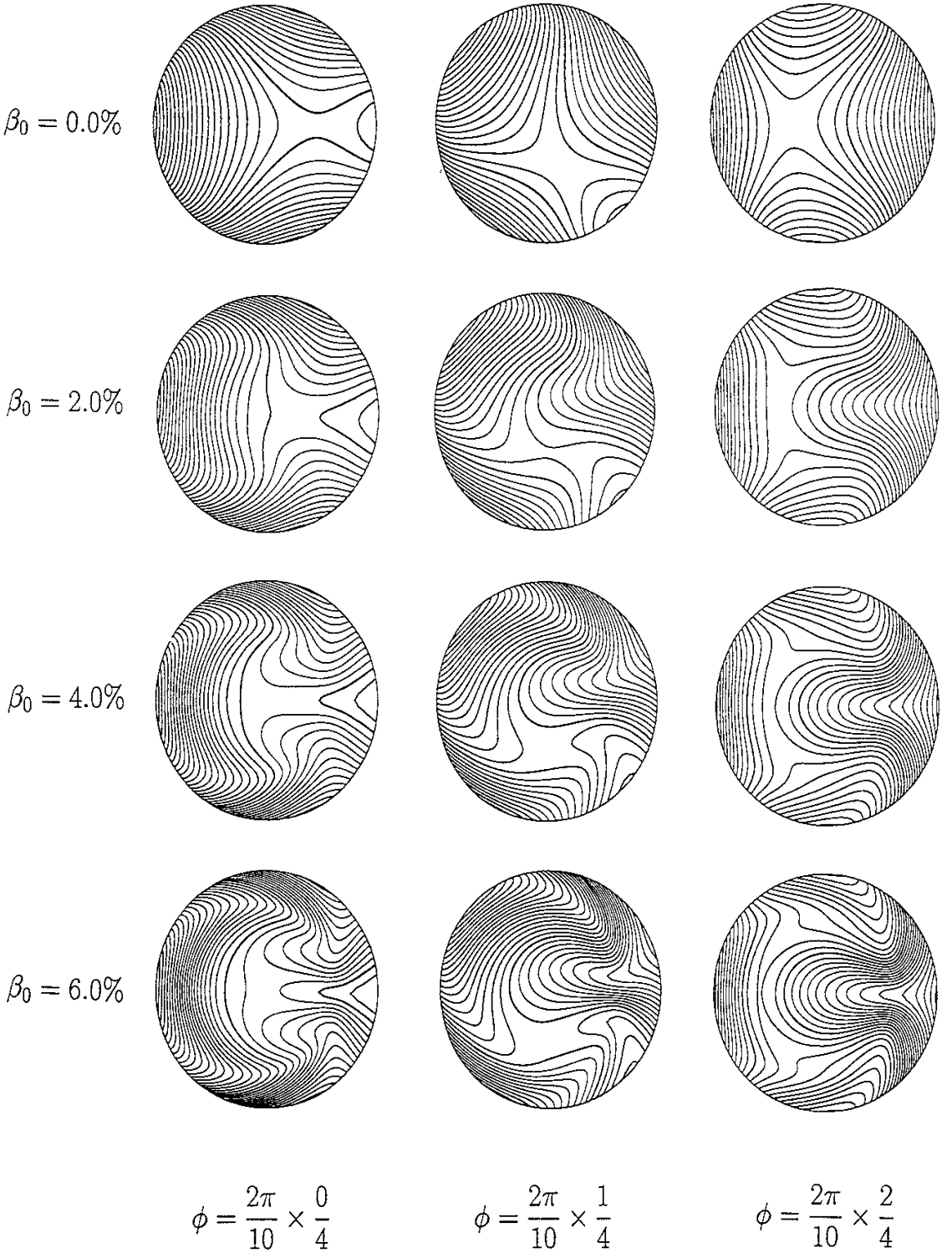
$\beta_0 = 0.0\%$
$\beta_0 = 2.0\%$
$\beta_0 = 4.0\%$
$\beta_0 = 6.0\%$
$\phi = \frac{2\pi}{10} \times \frac{0}{4}$
$\phi = \frac{2\pi}{10} \times \frac{1}{4}$
$\phi = \frac{2\pi}{10} \times \frac{2}{4}$

FIG. 1

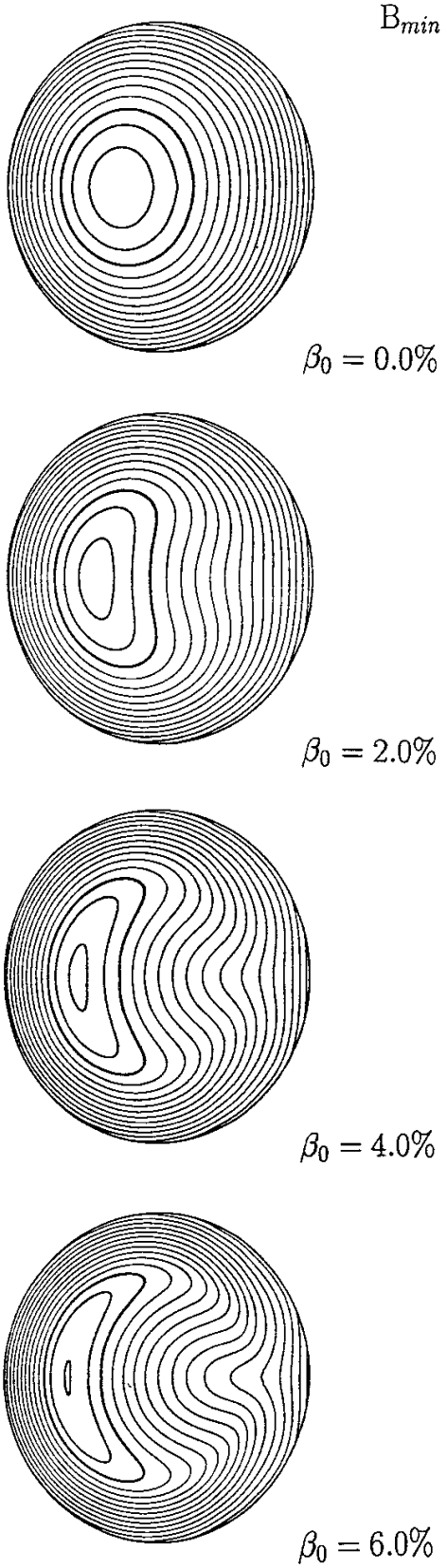

FIG. 2

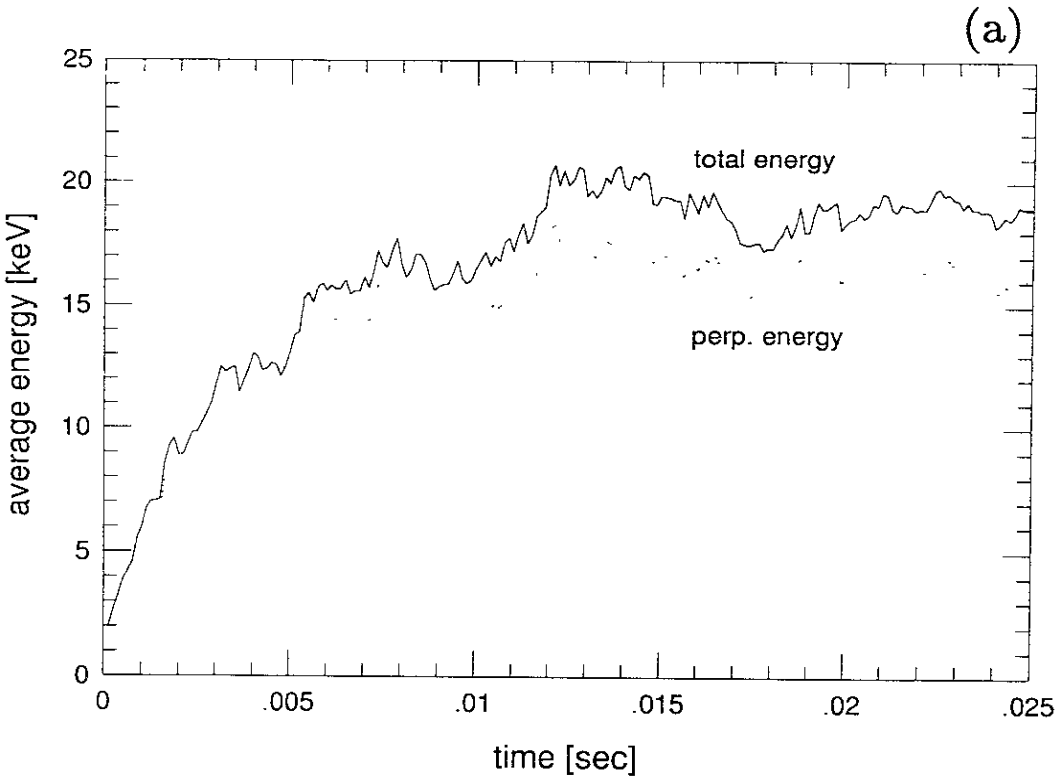
(a)
25
20
15
10
5
0
average energy [keV]
total energy
perp. energy
0
.005
.01
.015
.02
.025
time [sec]

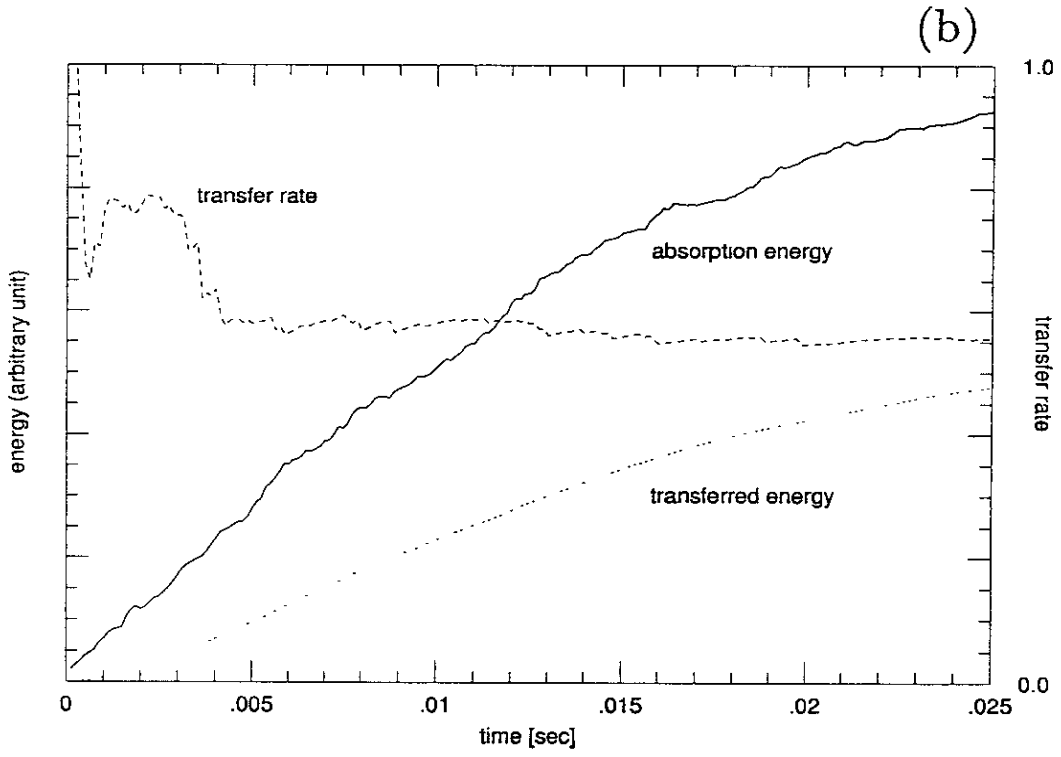
(b)
1.0
0.0
transfer rate
absorption energy
transferred energy
energy (arbitrary unit)
transfer rate
0
.005
.01
.015
.02
.025
time [sec]

FIG. 3

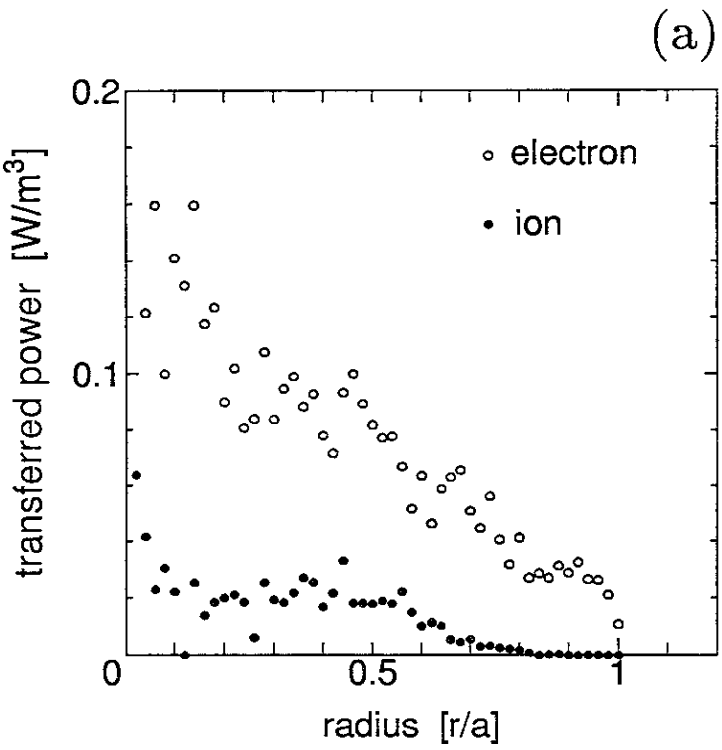
(a)
0.2
0.1
0
0.5
1
transferred power [W/m3]
radius [r/a]
electron
ion

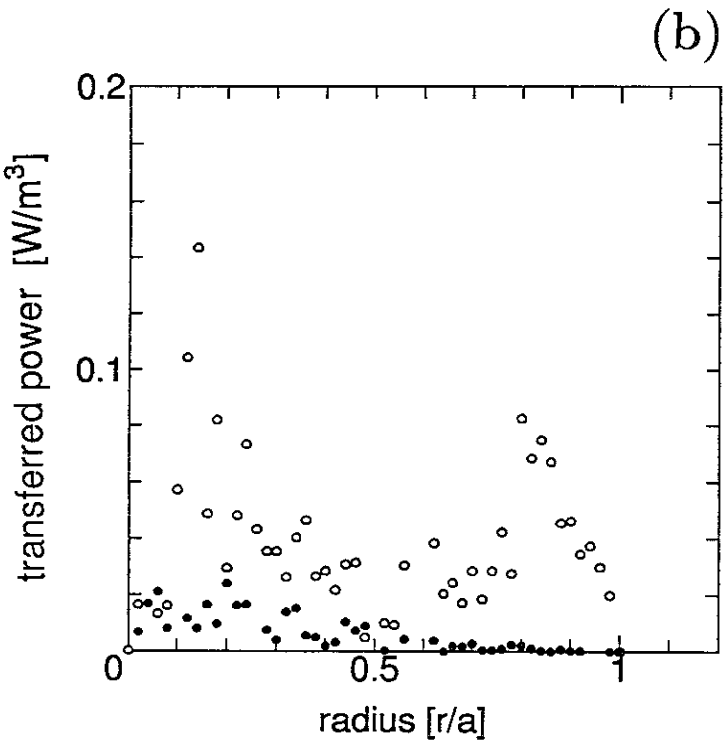
(b)
0.2
0.1
0
0.5
1
transferred power [W/m3]
radius [r/a]

FIG. 4

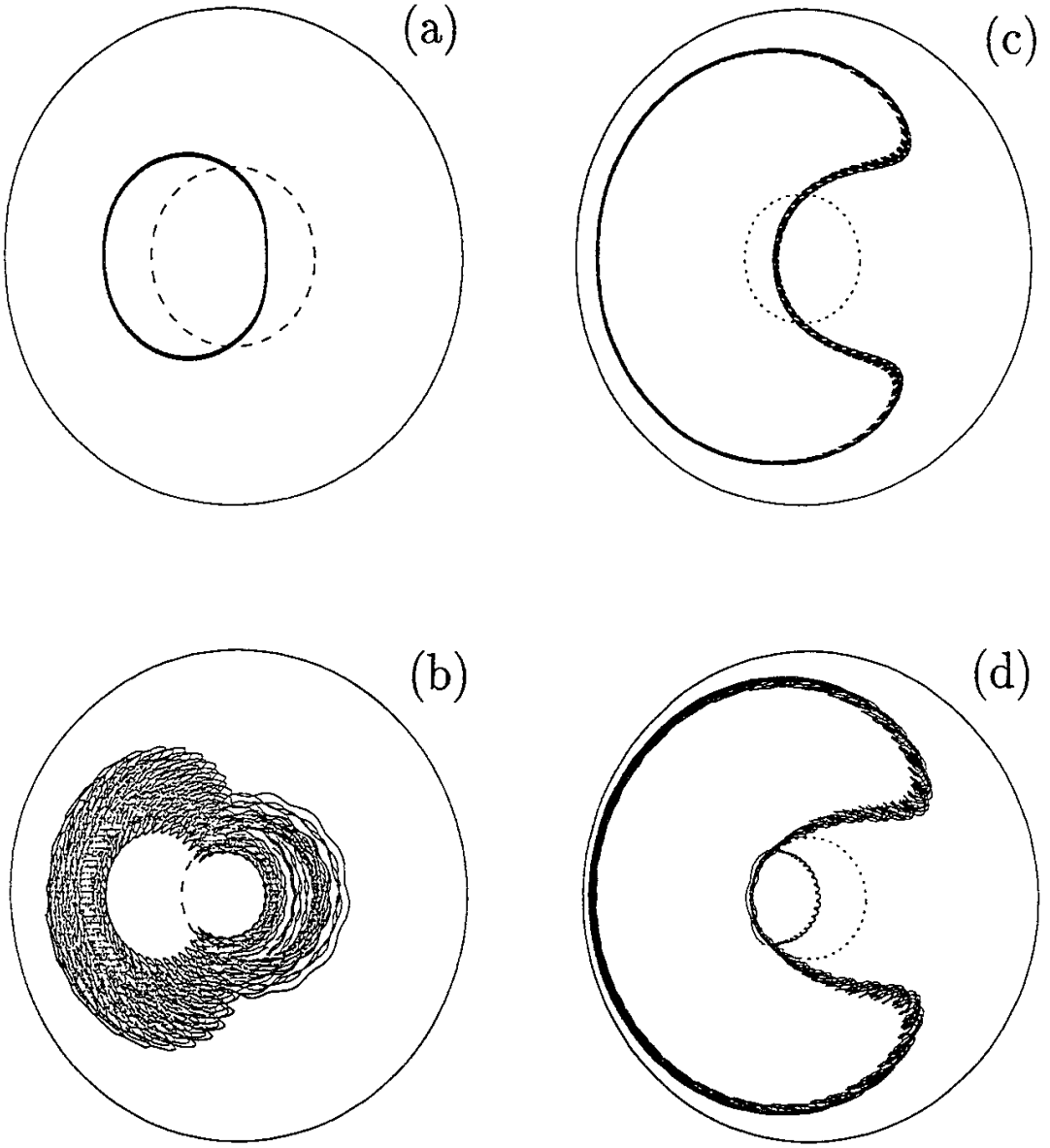

FIG. 5

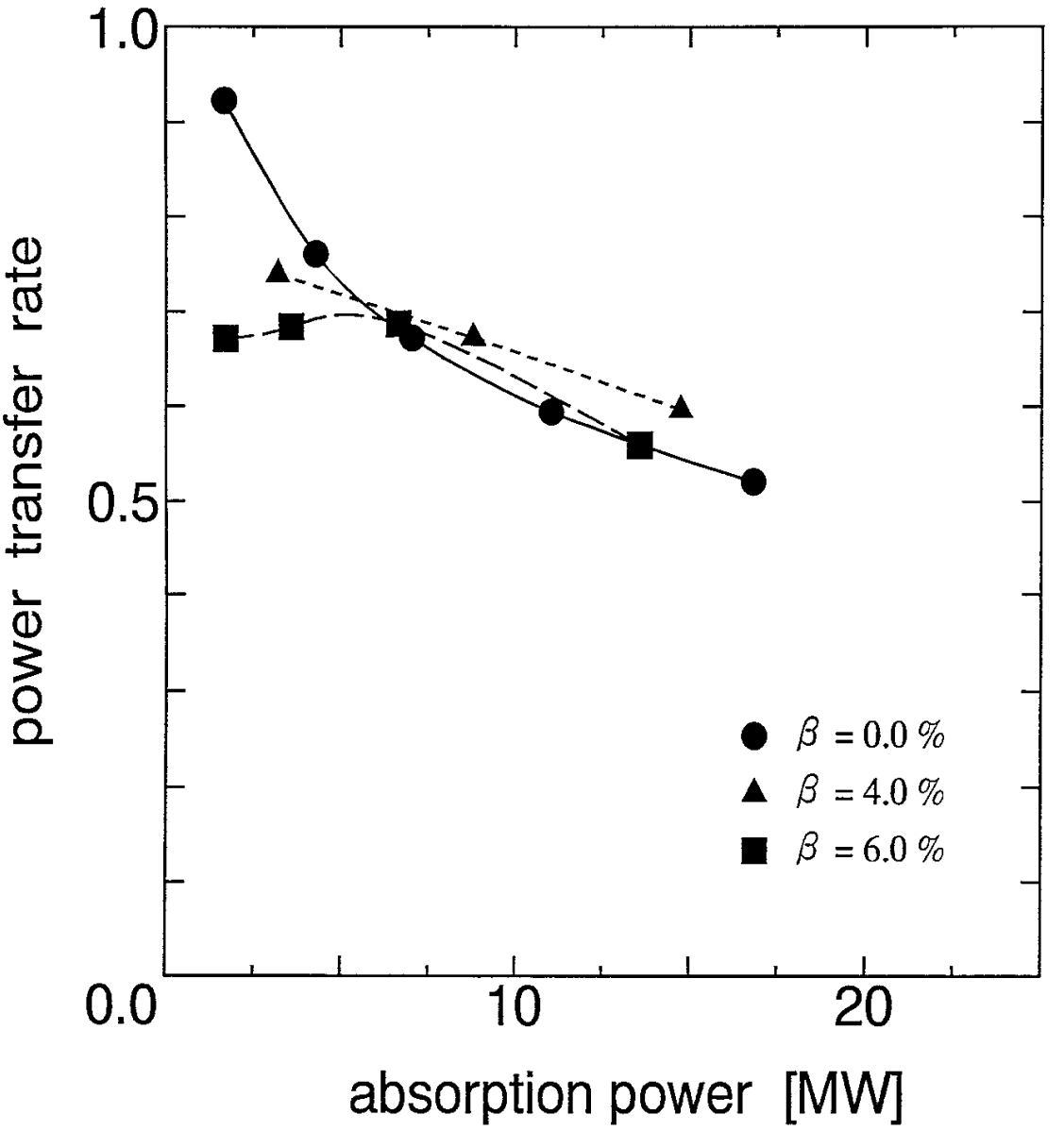
1.0
0.5
0.0
power transfer rate
10
20
absorption power [MW]
β = 0.0 %
β = 4.0 %
β = 6.0 %

FIG. 6

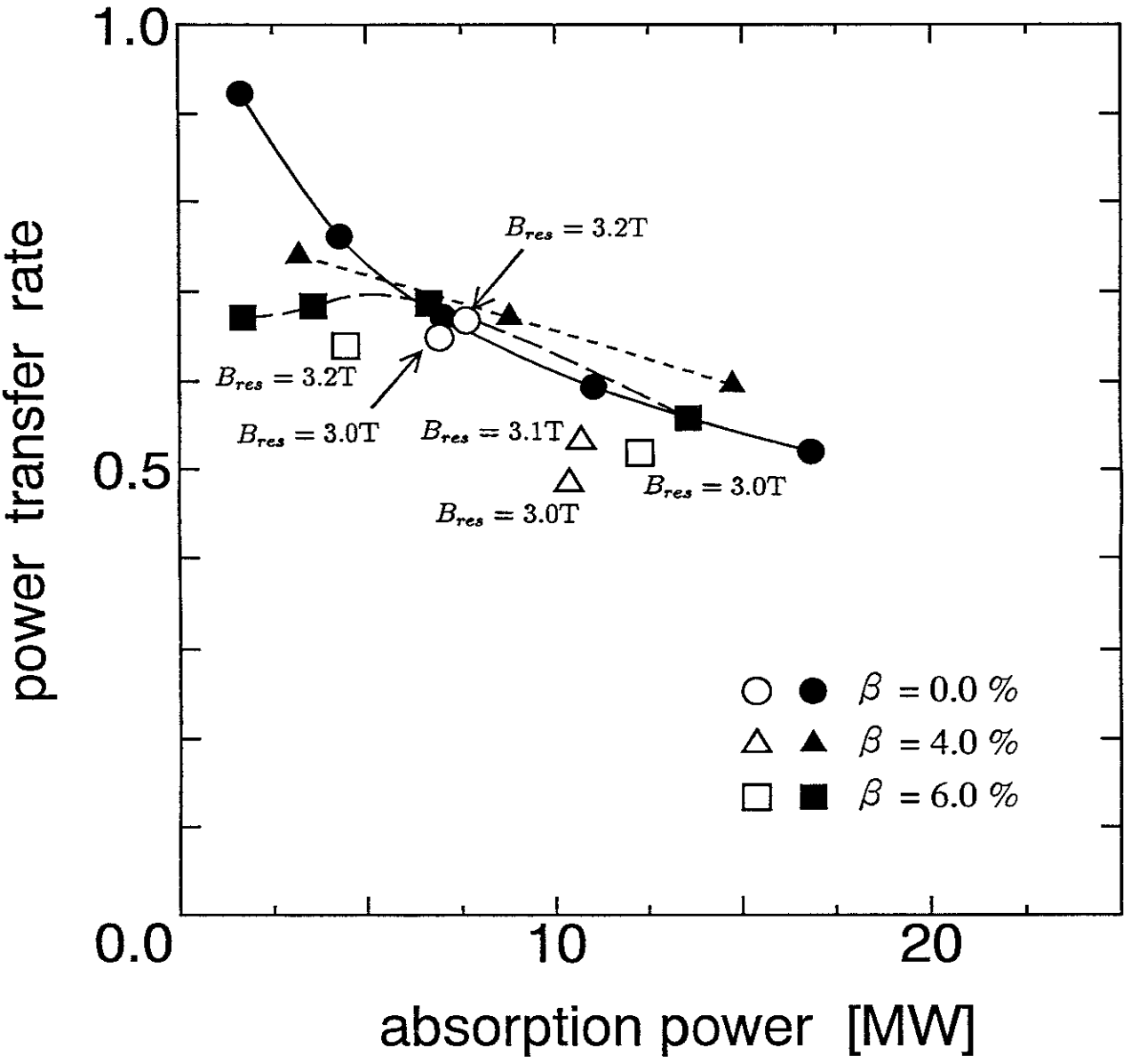
1.0
0.5
0.0
power transfer rate
10
20
absorption power [MW]
B_{res} = 3.2T
B_{res} = 3.2T
B_{res} = 3.0T
B_{res} = 3.1T
B_{res} = 3.0T
B_{res} = 3.0T
β = 0.0 %
β = 4.0 %
β = 6.0 %

FIG. 7

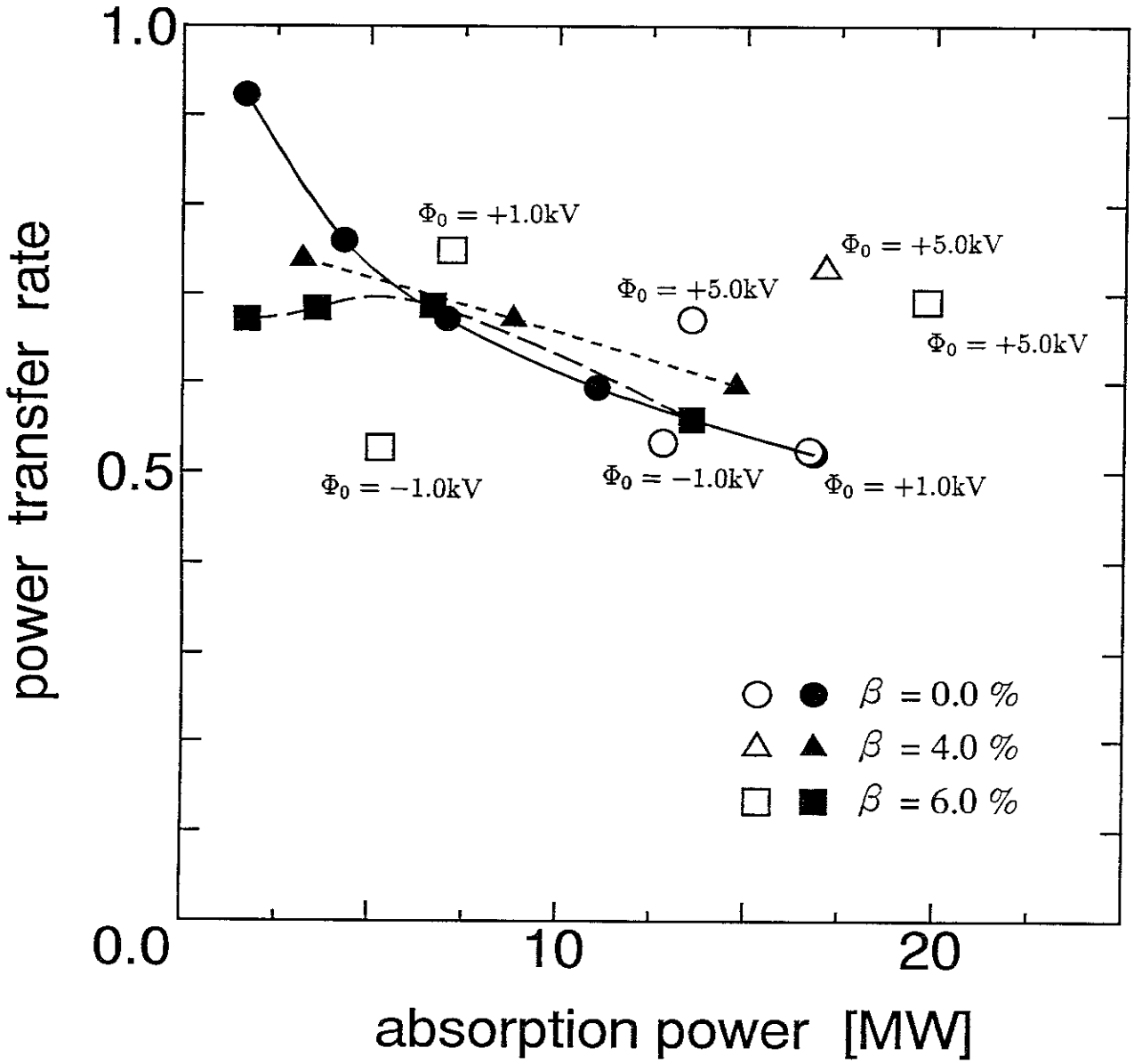
1.0
0.5
0.0
power transfer rate
10
20
absorption power [MW]
$\Phi_0 = +1.0$kV
$\Phi_0 = +5.0$kV
$\Phi_0 = +5.0$kV
$\Phi_0 = +5.0$kV
$\Phi_0 = -1.0$kV
$\Phi_0 = -1.0$kV
$\Phi_0 = +1.0$kV
$\beta = 0.0$ %
$\beta = 4.0$ %
$\beta = 6.0$ %

FIG. 8

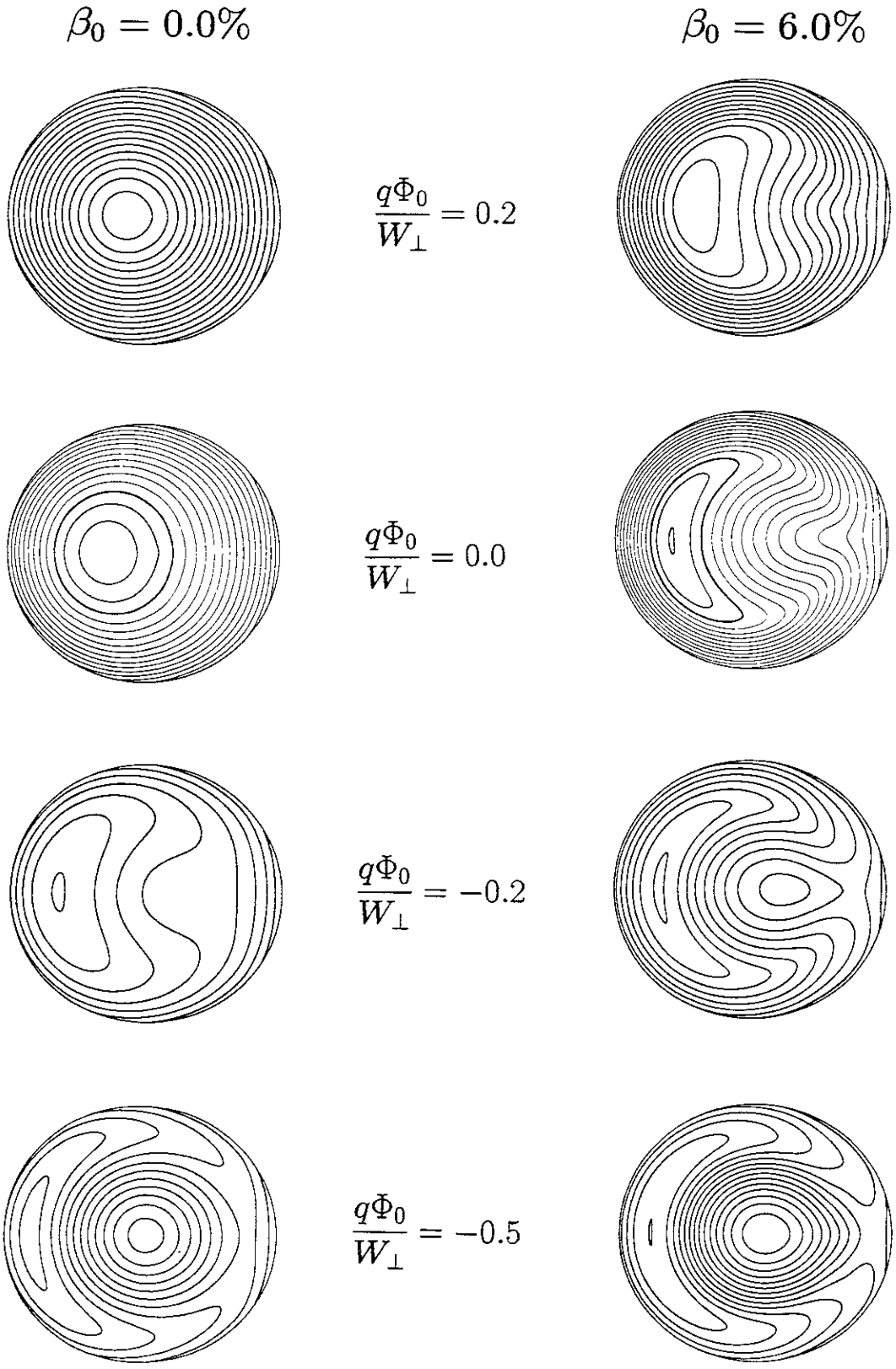
$\beta_0 = 0.0\%$
$\beta_0 = 6.0\%$
$\frac{q\Phi_0}{W_\perp} = 0.2$
$\frac{q\Phi_0}{W_\perp} = 0.0$
$\frac{q\Phi_0}{W_\perp} = -0.2$
$\frac{q\Phi_0}{W_\perp} = -0.5$

FIG. 9

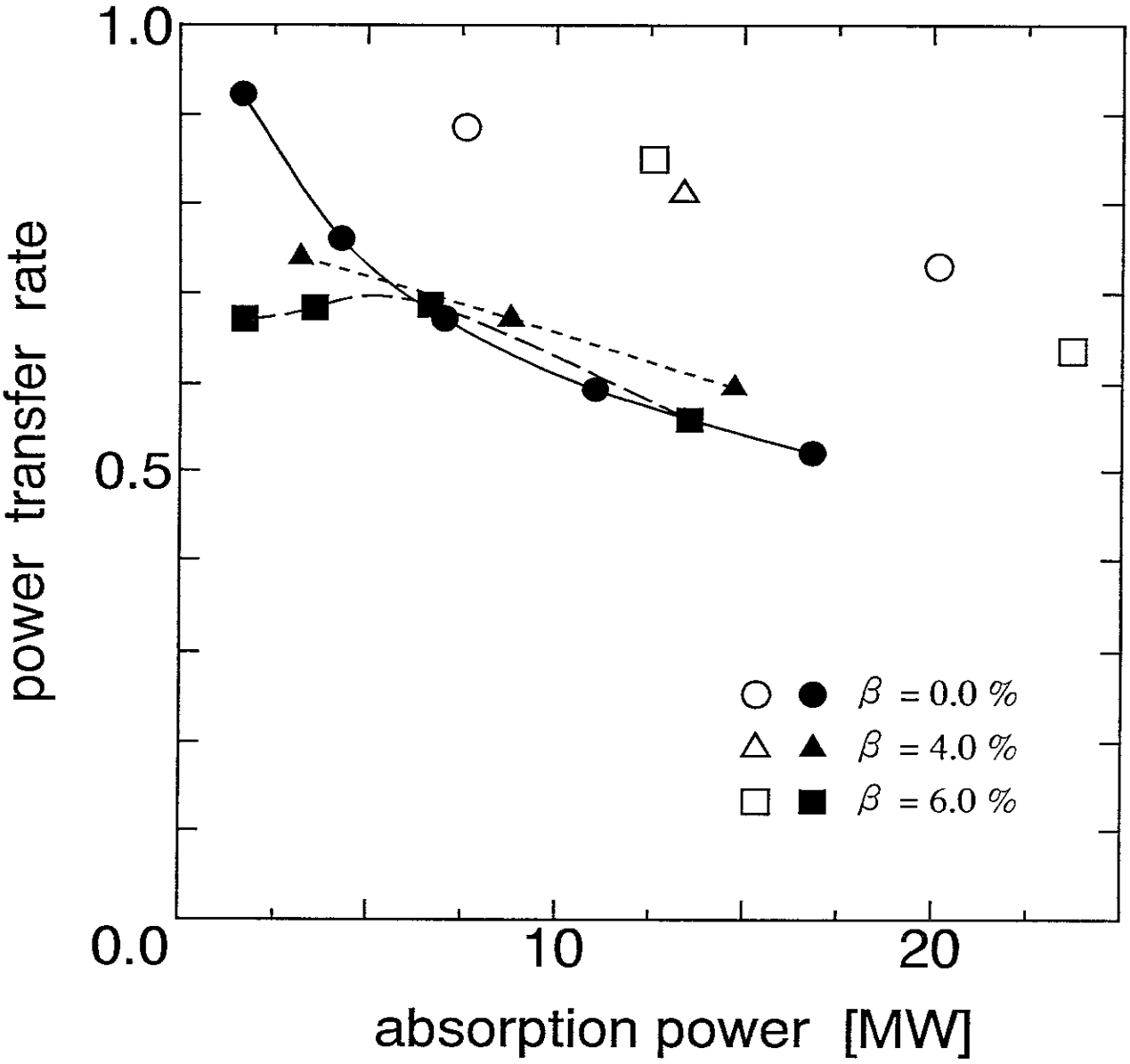
1.0
0.5
0.0
power transfer rate
10
20
absorption power [MW]
β = 0.0 %
β = 4.0 %
β = 6.0 %

FIG. 10

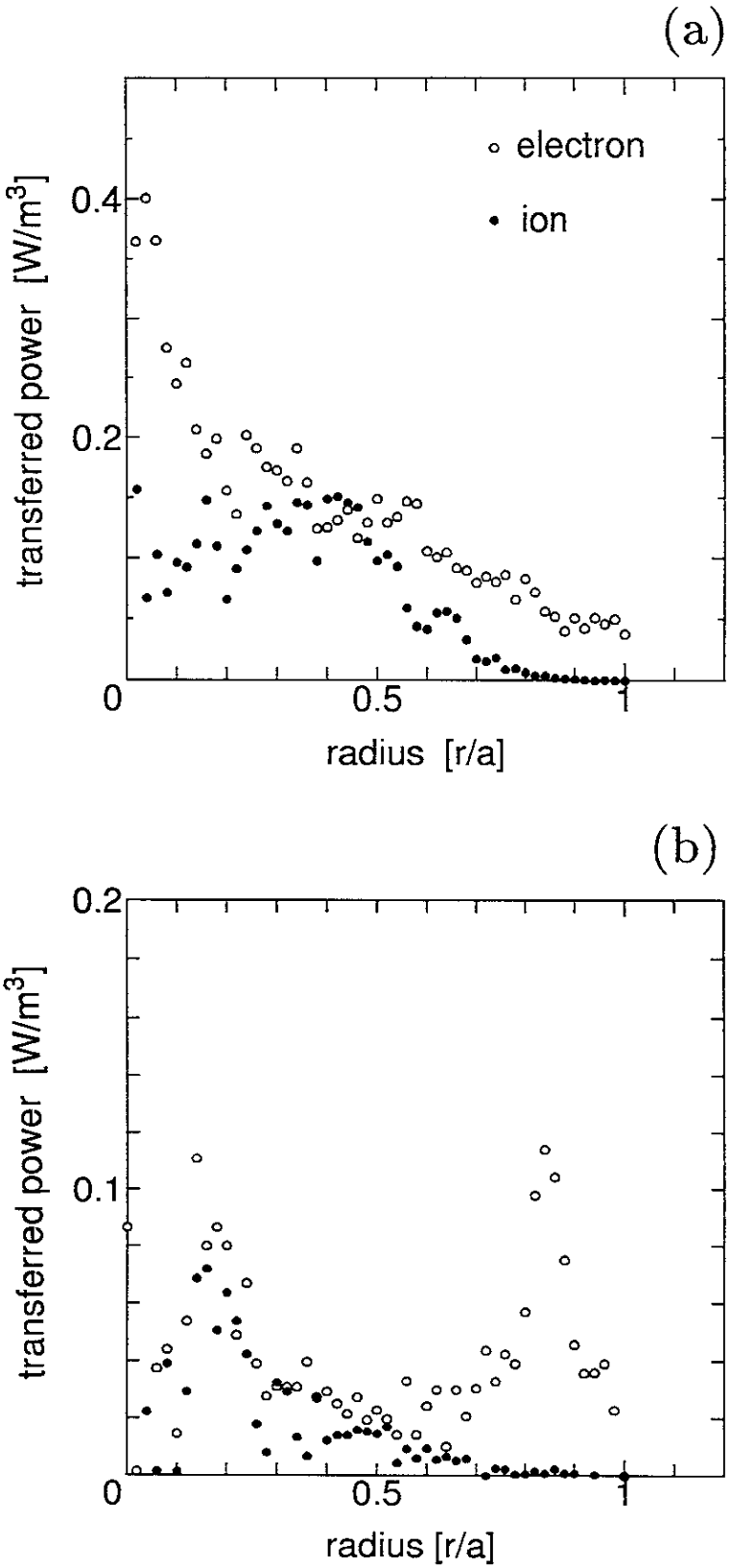
(a)
electron
ion
transferred power [W/m3]
0.4
0.2
0
0.5
1
radius [r/a]
(b)
0.2
0.1
transferred power [W/m3]
0
0.5
1
radius [r/a]

FIG. 11

Recent Issues of NIFS Series

NIFS-196 T. Mori, K. Akaishi, Y. Kubota, O. Motojima, M. Mushiaki, Y. Funato and Y. Hanaoka, *Pumping Experiment of Water on B and LaB_6 Films with Electron Beam Evaporator* ; Oct., 1992

NIFS-197 T. Kato and K. Masai, *X-ray Spectra from Hinotori Satellite and Suprathermal Electrons* ; Oct. 1992

NIFS-198 K. Toi, S. Okamura, H. Iguchi, H. Yamada, S. Morita, S. Sakakibara, K. Ida, K. Nishimura, K. Matsuoka, R. Akiyama, H. Arimoto, M. Fujiwara, M. Hosokawa, H. Idei, O. Kaneko, S. Kubo, A. Sagara, C. Takahashi, Y. Takeiri, Y. Takita, K. Tsumori, I. Yamada and H. Zushi, *Formation of H-mode Like Transport Barrier in the CHS Heliotron / Torsatron* ; Oct. 1992

NIFS-199 M. Tanaka, *A Kinetic Simulation of Low-Frequency Electromagnetic Phenomena in Inhomogeneous Plasmas of Three-Dimensions* ; Nov. 1992

NIFS-200 K. Itoh, S.-I. Itoh, H. Sanuki and A. Fukuyama, *Roles of Electric Field on Toroidal Magnetic Confinement*, Nov. 1992

NIFS-201 G. Gnudi and T. Hatori, *Hamiltonian for the Toroidal Helical Magnetic Field Lines in the Vacuum*; Nov. 1992

NIFS-202 K. Itoh, S.-I. Itoh and A. Fukuyama, *Physics of Transport Phenomena in Magnetic Confinement Plasmas*; Dec. 1992

NIFS-203 Y. Hamada, Y. Kawasumi, H. Iguchi, A. Fujisawa, Y. Abe and M. Takahashi, *Mesh Effect in a Parallel Plate Analyzer*; Dec. 1992

NIFS-204 T. Okada and H. Tazawa, *Two-Stream Instability for a Light Ion Beam -Plasma System with External Magnetic Field;* Dec. 1992

NIFS-205 M. Osakabe, S. Itoh, Y. Gotoh, M. Sasao and J. Fujita, *A Compact Neutron Counter Telescope with Thick Radiator (Cotetra) for Fusion Experiment*; Jan. 1993

NIFS-206 T. Yabe and F. Xiao, *Tracking Sharp Interface of Two Fluids by the CIP (Cubic-Interpolated Propagation) Scheme*, Jan. 1993

NIFS-207 A. Kageyama, K. Watanabe and T. Sato, *Simulation Study of MHD Dynamo : Convection in a Rotating Spherical Shell*; Feb. 1993

NIFS-208 M. Okamoto and S. Murakami, *Plasma Heating in Toroidal Systems*; Feb. 1993

NIFS-209 K. Masai, *Density Dependence of Line Intensities and Application to Plasma Diagnostics*; Feb. 1993

NIFS-210 K. Ohkubo, M. Hosokawa, S. Kubo, M. Sato, Y. Takita and T. Kuroda, *R&D of Transmission Lines for ECH System* ; Feb. 1993

NIFS-211 A. A. Shishkin, K. Y. Watanabe, K. Yamazaki, O. Motojima, D. L. Grekov, M. S. Smirnova and A. V. Zolotukhin, *Some Features of Particle Orbit Behavior in LHD Configurations*; Mar. 1993

NIFS-212 Y. Kondoh, Y. Hosaka and J.-L. Liang, *Demonstration for Novel Self-organization Theory by Three-Dimensional Magnetohydrodynamic Simulation*; Mar. 1993

NIFS-213 K. Itoh, H. Sanuki and S.-I. Itoh, *Thermal and Electric Oscillation Driven by Orbit Loss in Helical Systems*; Mar. 1993

NIFS-214 T. Yamagishi, *Effect of Continuous Eigenvalue Spectrum on Plasma Transport in Toroidal Systems*; Mar. 1993

NIFS-215 K. Ida, K. Itoh, S.-I.Itoh, Y. Miura, JFT-2M Group and A. Fukuyama, *Thickness of the Layer of Strong Radial Electric Field in JFT-2M H-mode Plasmas*; Apr. 1993

NIFS-216 M. Yagi, K. Itoh, S.-I. Itoh, A. Fukuyama and M. Azumi, *Analysis of Current Diffusive Ballooning Mode*; Apr. 1993

NIFS-217 J. Guasp, K. Yamazaki and O. Motojima, *Particle Orbit Analysis for LHD Helical Axis Configurations* ; Apr. 1993

NIFS-218 T. Yabe, T. Ito and M. Okazaki, *Holography Machine HORN-1 for Computer-aided Retrieve of Virtual Three-dimensional Image* ; Apr. 1993

NIFS-219 K. Itoh, S.-I. Itoh, A. Fukuyama, M. Yagi and M. Azumi, *Self-sustained Turbulence and L-Mode Confinement in Toroidal Plasmas* ; Apr. 1993

NIFS-220 T. Watari, R. Kumazawa, T. Mutoh, T. Seki, K. Nishimura and F. Shimpo, *Applications of Non-resonant RF Forces to Improvement of Tokamak Reactor Performances Part I: Application of Ponderomotive Force* ; May 1993

NIFS-221 S.-I. Itoh, K. Itoh, and A. Fukuyama, *ELMy-H mode as Limit Cycle and Transient Responses of H-modes in Tokamaks* ; May 1993

NIFS-222 H. Hojo, M. Inutake, M. Ichimura, R. Katsumata and T. Watanabe,

Interchange Stability Criteria for Anisotropic Central-Cell Plasmas in the Tandem Mirror GAMMA 10 ; May 1993

NIFS-223 K. Itoh, S.-I. Itoh, M. Yagi, A. Fukuyama and M. Azumi, *Theory of Pseudo-Classical Confinement and Transmutation to L-Mode;* May 1993

NIFS-224 M. Tanaka, *HIDENEK: An Implicit Particle Simulation of Kinetic-MHD Phenomena in Three-Dimensional Plasmas;* May 1993

NIFS-225 H. Hojo and T. Hatori, *Bounce Resonance Heating and Transport in a Magnetic Mirror;* May 1993

NIFS-226 S.-I. Iton, K. Itoh, A. Fukuyama, M. Yagi, *Theory of Anomalous Transport in H-Mode Plasmas;* May 1993

NIFS-227 T. Yamagishi, *Anomalous Cross Field Flux in CHS ;* May 1993

NIFS-228 Y. Ohkouchi, S. Sasaki, S. Takamura, T. Kato, *Effective Emission and Ionization Rate Coefficients of Atomic Carbons in Plasmas;* June 1993

NIFS-229 K. Itoh, M. Yagi, A. Fukuyama, S.-I. Itoh and M. Azumi, *Comment on 'A Mean Field Ohm's Law for Collisionless Plasmas;* June 1993

NIFS-230 H. Idei, K. Ida, H. Sanuki, H. Yamada, H. Iguchi, S. Kubo, R. Akiyama, H. Arimoto, M. Fujiwara, M. Hosokawa, K. Matsuoka, S. Morita, K. Nishimura, K. Ohkubo, S. Okamura, S. Sakakibara, C. Takahashi, Y. Takita, K. Tsumori and I. Yamada, *Transition of Radial Electric Field by Electron Cyclotron Heating in Stellarator Plasmas;* June 1993

NIFS-231 H.J. Gardner and K. Ichiguchi, *Free-Boundary Equilibrium Studies for the Large Helical Device,* June 1993

NIFS-232 K. Itoh, S.-I. Itoh, A. Fukuyama, H. Sanuki and M. Yagi, *Confinement Improvement in H-Mode-Like Plasmas in Helical Systems,* June 1993

NIFS-233 R. Horiuchi and T. Sato, *Collisionless Driven Magnetic Reconnection,* June 1993

NIFS-234 K. Itoh, S.-I. Itoh, A. Fukuyama, M. Yagi and M. *Azumi, Prandtl Number of Toroidal Plasmas;* June 1993

NIFS-235 S. Kawata, S. Kato and S. Kiyokawa , *Screening Constants for Plasma;* June 1993

NIFS-236 A. Fujisawa and Y. Hamada, *Theoretical Study of Cylindrical Energy*

Analyzers for MeV Range Heavy Ion Beam Probes; July 1993

NIFS-237 N. Ohyabu, A. Sagara, T. Ono, T. Kawamura and O. Motojima, *Carbon Sheet Pumping;* July 1993

NIFS-238 K. Watanabe, T. Sato and Y. Nakayama, *Q-profile Flattening due to Nonlinear Development of Resistive Kink Mode and Ensuing Fast Crash in Sawtooth Oscillations;* July 1993

NIFS-239 N. Ohyabu, T. Watanabe, Hantao Ji, H. Akao, T. Ono, T. Kawamura, K. Yamazaki, K. Akaishi, N. Inoue, A. Komori, Y. Kubota, N. Noda, A. Sagara, H. Suzuki, O. Motojima, M. Fujiwara, A. Iiyoshi, *LHD Helical Divertor;* July 1993

NIFS-240 Y. Miura, F. Okano, N. Suzuki, M. Mori, K. Hoshino, H. Maeda, T. Takizuka, JFT-2M Group, K. Itoh and S.-I. Itoh, *Ion Heat Pulse after Sawtooth Crash in the JFT-2M Tokamak;* Aug. 1993

NIFS-241 K. Ida, Y.Miura, T. Matsuda, K. Itoh and JFT-2M Group, *Observation of non Diffusive Term of Toroidal Momentum Transport in the JFT-2M Tokamak;* Aug. 1993

NIFS-242 O.J.W.F. Kardaun, S.-I. Itoh, K. Itoh and J.W.P.F. Kardaun, *Discriminant Analysis to Predict the Occurrence of ELMS in H-Mode Discharges;* Aug. 1993

NIFS-243 K. Itoh, S.-I. Itoh, A. Fukuyama, *Modelling of Transport Phenomena;* Sep. 1993

NIFS-244 J. Todoroki, *Averaged Resistive MHD Equations;* Sep. 1993

NIFS-245 M. Tanaka, *The Origin of Collisionless Dissipation in Magnetic Reconnection;* Sep. 1993

NIFS-246 M. Yagi, K. Itoh, S.-I. Itoh, A. Fukuyama and M. Azumi, *Current Diffusive Ballooning Mode in Seecond Stability Region of Tokamaks;* Sep. 1993

NIFS-247 T. Yamagishi, *Trapped Electron Instabilities due to Electron Temperature Gradient and Anomalous Transport;* Oct. 1993

NIFS-248 Y. Kondoh, *Attractors of Dissipative Structure in Three Disspative Fluids;* Oct. 1993